Research Article

Nano Research
2022, 15(10): 9082–9091

ISSN 1998-0124 CN 11-5974/O4
https://doi.org/10.1007/s12274-022-4542-9

Versatile nanocomposite augments high-intensity focused ultrasound for high-efficacy sonodynamic therapy of glioma

Yingyan Zheng[1,2,§], Dejun She[1,2,§], Huihui Huang[5,§], Lin Lin[2], Sunhui Chen[3], Yiping Lu[2], Li Liu[4] (✉), Zhiqing Pang[3] (✉), and Bo Yin[2] (✉)

[1] *Department of Radiology, First Affiliated Hospital of Fujian Medical University, Fuzhou 350004, China*
[2] *Department of Radiology, Huashan Hospital, Fudan University, Shanghai 200040, China*
[3] *Department of Pharmaceutics, School of Pharmacy, Fudan University, Key Laboratory of Smart Drug Delivery Ministry of Education, Shanghai 201203, China*
[4] *Department of Radiology, Shanghai Cancer Center, Fudan University, Shanghai 200032, China*
[5] *Department of Pharmacology, School of Pharmacy, Fujian Medical University, Fuzhou 350108, China*
[§] *Yingyan Zheng, Dejun She, and Huihui Huang contributed equally to this work.*

Received: 12 February 2022 / **Revised:** 15 May 2022 / **Accepted:** 16 May 2022

ABSTRACT

High-intensity focused ultrasound (HIFU), with inherent advantages of improved ultrasonic depth and low off-target damage, holds the promising capability for glioma treatment, but the relatively long therapeutic time and potential physical complications may hamper its clinical application. Herein, a bovine serum albumin (BSA)-based nanoplatform with *in situ* growth of MnO_2 was synthesized, and Protoporphyrin IX (PpIX) was further anchored to obtain a versatile PpIX@MnO_2@BSA nanoplatform (denoted as BMP). By employing HIFU as the exogenous irradiation source, a high-efficacy sonodynamic therapy (SDT) is developed, in which the excited BMP enables the production of tumoricidal reactive oxygen species (ROS). The inherent tumor microenvironment (TME)-responsive property of MnO_2 endows BMP with specific T_1-weighted magnetic resonance imaging (MRI) by releasing Mn^{2+}, and the simultaneously generated O_2 facilitates hypoxia alleviation as well as $^1O_2$ generation. Compared with HIFU therapy alone, suppression of glioma growth and improved survival benefits are achieved through the designed TME-responsive nanocomposite under HIFU exposure. The high-efficacy SDT strategy combining BMP and HIFU demonstrated favorable TME-responsive T_1-weighted MRI, hypoxic environment alleviation, and anti-tumor capability, providing a perspective paradigm for MRI-guided glioma treatment.

KEYWORDS

glioma, sonodynamic therapy, high intensity focused ultrasound, tumor microenvironment, responsive magnetic resonance imaging

1 Introduction

Glioma, the most frequent primary neoplasms of the central nervous system (CNS), is characterized with varied managements and prognoses [1–3]. Although considerable developments have been recently achieved in surgery, chemotherapy, and radiotherapy, conventional therapeutic effects are often plagued by complicated tumor progression, recurrence, and chemo/radio-resistance, thereby compromising the overall survival of patients with glioma [2, 4]. High-intensity focused ultrasound (HIFU) is a developing micro-invasive modality with precise ultrasonic energy delivery and decreased attenuation, which has been arguably reported to hold the promising possibility for treating intracranial glioma [5, 6]. It lessens dissipation during propagation, enhances spatio-temporal depth and, ultimately, offers incisionless on-target eradication with vicinity spared [7, 8]. However, relative long sonication time is often required for HIFU therapy alone on account of a narrow treatment envelope, which contributes to the increased risk of physical complications such as risen body temperature, highlighting the urgent requirement to improve its efficacy and bio-safety [9].

Sonodynamic therapy (SDT), a non-invasive modality involving sonosensitizer to generate tumoricidal reactive oxygen species (ROS), principally singlet oxygen ($^1O_2$), under ultrasound (US) exposure in routine practice, possesses the alternative substitutability in cancer eradication [10–14]. Based on the activation of chemical sonosensitizer, SDT could induce cellular apoptosis in a site-directed manner [13]. However, certain inherent limitations of conventional SDT, such as insufficient ultrasonic penetration and reliance of abundant oxygen (O_2), may hamper its further clinical application in glioma treatment [14, 15]. Conceivably, the employment of HIFU, as an exogenous excitation source, could improve the therapeutic efficiency of conventional SDT by decreasing ultrasonic dissipation. Moreover, combining HIFU with sonosensitizer would create a synergistic effect, in which sonosensitizer is capable of converting non-toxic O_2 into those harmful ROS when irradiated by HIFU, and therefore, it carries the potential to shorten acoustic time in support of the high-efficacy SDT.

Address correspondence to Li Liu, llbbsy@163.com; Zhiqing Pang, zqpang@fudan.edu.cn; Bo Yin, yinbo@fudan.edu.cn

Modern imaging techniques are crucial for HIFU-associated therapy to visualize tumor location and guide treatment time [5, 16]. Magnetic resonance imaging (MRI) has been widely performed for integrated intervention procedure, due to its favorable anatomic resolution, non-ionizing radiation, and objective repeatability [5, 17]. Contrast agents (CAs), such as gadolinium (Gd)-based CAs, are commonly administrated to improve MRI diagnostic accuracy, but they are "always-on" enhancement with lower specificity, promoting numerous translational researches towards the replaceable candidates [18, 19]. Manganese (Mn)-based CAs, especially manganese dioxide (MnO_2) nanoparticles, have been explored extensively in the past few years, owing to their immanent responsive property to the special tumor microenvironment (TME) that featured with weak acidity and hydrogen peroxide (H_2O_2)/glutathione (GSH) overproduction [20–22]. Based on the reactivity with H_2O_2, MnO_2 can simultaneously generate Mn^{2+} and O_2 in the TME, rendering activatable T_1-weighted contrast effects to enhance distinction between glioma and surrounding structures [23–26]. Moreover, except hypoxic environment alleviation, the supplied O_2 can further enable sonosensitizer to ulteriorly produce $^1O_2$ under HIFU irradiation, attributing to selective cancerous tissue destruction [27–29]. Thus, MRI-guided high-efficacy SDT, with MnO_2 as the CAs, can be considered as an ideal way for glioma treatment.

In order to improve water solubility as well as pharmacokinetic property, various nanocarriers, including endogenous and exogenous ones, have been designed and developed for molecules delivery [30–32]. Owing to their intrinsic biological security and low immunogenicity, endogenous nanovehicles are in widespread explored [30]. In addition to the aforementioned characters, albumin, representing the most abundant plasma protein, also displays satisfactory stability, long half-life in blood circulation as well as versatile modification [33–42]. Besides, albumin-based nanoplatforms, mainly constructed from bovine serum albumin (BSA) or human serum albumin (HSA), can be easily and inexpensively synthesized under mild conditions through biomineralization, covalent conjugation, or hydrophobic interaction [43]. Hence, albumin-based multifunctional nanoplatforms have been aroused intensive interest in the field of tumor theranostics given their admirable advantages.

With regard to these factors, a BSA-based nanoplatform was designed for TME responsive MRI-guided SDT of glioma (Scheme 1). The MnO_2 nanocrystals grown in BSA nanocarrier (MnO_2@BSA, denoted as BM) provided self-enhanced T_1-weighted MRI capability for pretreatment guidance, as well as simultaneous O_2 production for hypoxia alleviation and ROS generation. Protoporphyrin IX (PpIX), a common sonosensitizer, was further introduced to obtain PpIX@MnO_2@BSA nanoparticle (denoted as BMP) to produce noxious $^1O_2$ under HIFU irradiation. The prepared BMP realized satisfactory biosafety, imaging, and therapeutic efficiency both *in vitro* and *in vivo* experiments, eliciting the potential application of high-efficacy SDT combining with HIFU and sonosensitizer in treating glioma.

2 Experimental

2.1 Materials

BSA (≥ 98%) was obtained from Baomanbio (Shanghai, China). Manganese chloride tetrahydrate ($MnCl_2{\cdot}4H_2O$) and sodium hydroxide (NaOH) were ordered from Sinopharm Chemical Reagent Co., Ltd. (Shanghai, China). N,N-Dimethylformamide (DMF), 1-ethyl-3-(3-dimethyl-aminopropyl) carbodiimide hydrochloride (EDC·HCl), N-hydroxy succinimide (NHS), 2,7-dichlorofluorescin diacetate (DCFH-DA), and fluorescein isothiocyanate (FITC) were purchased from Sigma-Aldrich (St. Louis, USA). PpIX (≥ 95%) was from Shanghai Yuanye Bio-Technology Co., Ltd. (Shanghai, China). H_2O_2 (30%) was brought from Aladdin (Shanghai, China). Single oxygen sensor green (SOSG) and Dulbecco's modified Eagle medium (DMEM/high glucose) were provided by Thermo Fisher Scientifc Co., Ltd. (MA, USA). Fetal bovine serum (FBS), penicillin-streptomycin solution, and trypsin-ethylene diamine tetraacetic acid (trypsin-EDTA, 0.05%) were acquired from Life Science (Gibco™, Pittsburgh, USA). Calcein-AM and propidium iodide (PI) apoptosis detection kit, hydrogen peroxide assay kit, and 4,6-diamidino-2-phenylindole dihydrochloride (DAPI) were obtained from Beyotime Biotechnology (Shanghai, China). Hypoxyprobe kit was from Maokang Biotechnology Co., Ltd. (Shanghai, China). AnaeroPack™-Anaero and Anaero-indicator were acquired from MITSUBISHI GAS CHEMICAL COMPANY, INC (Japan).

2.2 Cells and animals

C6 cells were obtained from Chinese Academy of Sciences Cell Bank (Shanghai, China). The cells were incubated in DMEM

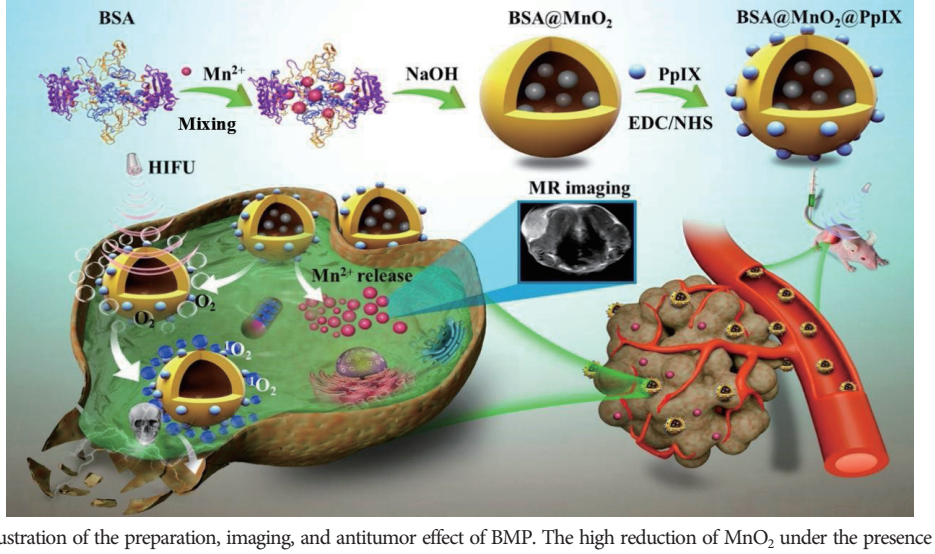

Scheme 1 Schematic illustration of the preparation, imaging, and antitumor effect of BMP. The high reduction of MnO_2 under the presence of H_2O_2 contributes in TME-responsive T_1-weighted MR imaging. Under HIFU irradiation with MRI guidance, BMP alleviates hypoxic environment by releasing O_2, and further facilitates the generation of toxic ROS to enhance the suppression of glioma growth, thereby realizing the high-efficacy SDT.

medium supplemented with 10% FBS and 1% penicillin-streptomycin solution under a humidity atmosphere containing 5% CO_2 at 37 °C. BALB/c nude mice (male, 6–8 weeks old, and 20 ± 2 g) and Sprague–Dawley (SD) rats (male, 6–8 weeks old, and 200 ± 20 g) were provided by BK lab (Shanghai, China). The animal study protocol was approved by the Institutional Animal Care and Use Committee at Fudan University.

2.3 Synthesis and characterization of BMP

BM was firstly constructed *in situ* synthesis procedure via biomineralization. In brief, 60 mg of BSA was dissolved in 30 mL of double distilled water (DDW), followed by the addition of 1 mL of $MnCl_2$ under magnetic stirring. After 5-min mixing, the solution pH was adjusted to 10 with NaOH solution meticulously, and the products were subsequently dialyzed for 2 days after 1 h reaction. Different Mn contents (0.01, 0.04, 0.08, and 0.1 M) were designed to evaluate the optimized input. Besides, the growth process of MnO_2 was monitored at varying timepoints with an ultraviolet–visible (UV–vis) spectrum (SHIMADZU UV-3600 spectrophotometer, Japan).

To obtain an activated PpIX solution, 2.4 mg PpIX, 2.4 mg EDC·HCl, and 1.44 mg NHS were dispersed in 2 mL of DMF in the dark. After 2 h magnetic stirring, the mixture was added dropwise to the 30 mL of BM solution (2 mg/mL) for further 6 h reaction to acquire the BMP. Those superfluous materials were sequentially removed by dialysis for 2 days. The solution was lyophilized and stored away from light for the following experiments. The hydrodynamic size and zeta potential were measured using a Malvern Instrument (Nano ZS90, UK). Transmission electron microscopy (TEM) (Tecnai G2 20 TWIN, USA) was adopted to observe the morphology. X-ray diffraction (XRD) was performed with a MiniFlex600 (Rigaku, Japan). The elemental valence state was investigated by X-ray photoelectron spectroscopy (XPS) (Thermo Scientific K-Alpha, USA). Thermogravimetric analyser (TGA) (TA Instruments Q500, USA) was performed to ascertain the amount of coupled PpIX on BMP nanoplatform. The spectra of different nanoparticles were assessed using the aforementioned UV–vis spectrum. The fluorescence intensity of nanoparticle was estimated with a fluorescence spectrophotometer (FS) (SHIMADZU RF-5301, Japan). Assessment of hydrodynamic size and UV–vis spectrum were conducted at different timepoints to evaluate the stability in various conditions.

The MnO_2-relevant H_2O_2 consumption experiment was conducted with the hydrogen peroxide assay kit. The reduction in H_2O_2 content (with an initial concentration of 100 μM) was measured quantitatively in the presence of BMP with different concentrations (0.05, 0.1, or 0.2 mg/mL) under the weak acid environment (pH = 6.5). To evaluate the H_2O_2-triggered degradation, BMP (at a final concentration of 0.25 mg/mL) was dissolved in phosphate buffer saline (PBS) or H_2O_2-containing PBS with different pH values (pH = 6.5 or 7.4), and shaken at a speed of 300 rpm at 37 °C to simulate the internal environment. The UV–vis spectrum was employed to record their spectra at varying time. In addition, the impact of pH values and the presence of H_2O_2 on O_2 generative capacity of BMP were estimated every 10 s by a dissolved oxygen analyzer (JPBJ-609L, INESA Instrument, China). SOSG, a selective fluorescence probe for $^1O_2$ detection, was utilized to assess ROS generation of BMP under H_2O_2 and different pH conditions (pH = 6.5 or 7.4), with or without US irradiation, and their fluorescence intensities were measured on the FS. Three groups, including US+H_2O_2 group, BMP group, and BMP+US+H_2O_2 group, were categorized, and $^1O_2$ production was quantified by an electron spin resonance (ESR) (JEOL-FA200, Japan).

2.4 MRI tests *in vitro* and *in vivo*

The responsive MRI ability of BMP *in vitro* and *in vivo* was all tested with a 3.0-Tesla MR system (Discovery MR750, GE Medical System, USA). T_1 mapping sequence was examined to elucidate the T_1 signals of BMP solutions collected in 5 mL of centrifuge tubes with varied Mn concentrations (6.25, 12.5, 25, 50, and 100 μM) at different pH values (pH = 7.4, 6.5, or 5.0), with or without H_2O_2. The sequence parameters were as follows: repetition time (TR)/echo time (TE) = 5,000 ms/7.9 ms, field of view (FOV) = 70 mm × 70 mm, matrix = 256 × 128, slice thickness (ST) = 2 mm, gap thickness (GT) = 2 mm, and inversion time (TI) = 50/100/200/500/800/1,200/1,500 ms. The region of interest (ROI) was drawn inside samples manually to measure T_1 value and determine the longitudinal relaxation rate (r_1).

To investigate the self-enhanced MRI capacity in glioma cells, C6 cells were cultured with DMEM medium or BMP-containing medium (100 μg/mL) for 4 h. Then, cells were collected and resuspended in PBS in 5 mL of centrifuge tubes for T_1-weighted imaging using the following parameters: TR/TE = 1,500 ms/12.8 ms, FOV = 70 mm × 70 mm, matrix = 256 × 128, and ST/GT = 2 mm/2 mm. Their imaging performances were compared with free DMEM medium as well as BMP solution. Besides, cells were incubated with BMP-containing media at different concentrations (12.5, 25, 50, 100, or 200 μg/mL) or culture time (0, 0.5, 1, 2, or 4 h) to explore the factors influenced on imaging performance. The ROIs were delineated on the samples and background to calculate signal noise ratio (SNR).

The orthotopic and subcutaneous glioma models were established in rats and nude mice for MRI evaluation *in vivo*, respectively. Rats were divided into BMP group (at an injected Mn dose of 0.1 mmol/kg) and gadolinium-gadopentetic acid (Gd-DTPA) group (at an injected Gd dose of 0.1 mmol/kg) randomly. T_1-weighted images (T_1WI) was performed at pre- and post-intravenous injection (5, 30, 60, 120, and 240 min) under the following parameters: TR/TE = 600 ms/12 ms, FOV = 90 mm × 70 mm, matrix = 192 × 192, and ST/GT = 2 mm/2 mm. Mice were injected with BMP at a Mn dose of 5 mg/kg and scanned at pre- and post- intravenous injection (0.5, 1, 2, 4, and 24 h). The parameters of T_1WI were set as follows: TR/TE = 700 ms/12 ms, FOV = 60 mm × 60 mm, matrix = 256 × 256, and ST/GT = 2 mm/2 mm. The ROIs were drawn on the tumors and muscles to determine SNR, and contrast to noise ratio (CNR) was defined as the ratio between the SNRs of tumor and muscle.

2.5 Cell toxicity *in vitro*

The influences of BMP concentration at different cultured environments, HIFU intensities, and HIFU durations on cell viability were estimated. C6 cells were planted on 96-well plates with a density of 7×10^3 cells/well. After 24-h incubation, the cells were treated with BMP-containing media at gradient concentrations (0, 25, 50, 100, 200, 400, 600, or 800 μg/mL) under simulative physiological environment (pH = 7.4) or TME (pH = 6.5 and 100 μM H_2O_2), or HIFU irradiation at varied intensities (2.8, 8.5, or 9.3 W/cm^2) and durations (1, 1.5, 2, 3, or 4 min). The cell counting kit-8 (CCK-8) assay was conducted after 24 h to assess the cell viability.

2.6 Cellular uptake study

C6 cells were cultured for 24 h in confocal dishes at a density of 1×10^5 cells/well for confocal laser scanning microscope (CLSM) (Olympus Company FV1000, Japan) observation or 6-well plates at a density of 2×10^5 cells/well for flow cytometry analysis (BD FACSAria II, USA). Afterwards, the media were replaced by FITC-

labelled BMP-containing media (200 μg/mL) and incubated for 0, 1, 2, or 4 h, respectively. The cells seeded in confocal dishes were further fixated by paraformaldehyde for 10 min and stained by DAPI for 30 min.

2.7 Cellular apoptosis assay

7×10^3 C6 cells were cultured in each 96-well plate. After 24 h, the substituted media with H_2O_2 (100 μM) and varying BMP concentrations (0, 25, 50, 100, or 200 μM) in different pH conditions (pH = 7.4 or 6.5) were added. Cells were subsequently treated with HIFU and the cell viability was appraised with the CCK-8 assay.

To qualitatively elucidate the therapeutic effect, C6 cells were seeded in confocal dishes at a density of 2×10^5 and incubated for 24 h. Five groups, including control group, HIFU group, BMP+H_2O_2+pH7.4 group, BMP+H_2O_2+HIFU+pH7.4 group, and BMP+HIFU+H_2O_2+pH6.5 group, were classified. The experimental procedure was set as a BMP concentration of 200 μg/mL, H_2O_2 concentration of 100 μM, and HIFU power of 8.5 W/cm^2 with a duration of 1.5 min. Calcein-AM (10 mM) and PI (2 mM) were stained for 30 min after managements, and the cellular apoptosis was imaged by CLSM.

2.8 Detection of ROS generation

C6 cells were seeded in 6-well plates and grouped identical to those in the above cellular apoptosis qualitative experiment. DAPI was adopted to stain the cell nuclei, followed by incubation of DCFH-DA (25 μM) for 30 min. The $^1O_2$ production was investigated by an inverted fluorescence microscope (Olympus, Japan). Semiquantitative analysis was performed to determine the relative fluorescence intensity for ROS production with the ImageJ software (version 1.8.0, National Institutes of Health, USA).

2.9 Pharmacokinetic, distribution, and biocompatibility studies *in vivo*

For biocompatibility study, healthy BALB/c mice were intravenously treated with 100 μL BMP (20 mg/mL), while a control group was set and injected with equivalent normal saline (NS). Mice were weighted and monitored every other day for 2 weeks. Their orbital blood and major organs were collected after observation for hemanalysis as well as hematoxylin-eosin (H&E) staining. For pharmacokinetic study, healthy BALB/c mice were administered with 100 μL BMP with a Mn dose of 5 mg/kg via the tail vein. Blood from the orbit was collected at several time points after injection and dissociated for inductively coupled plasma optical emission spectrometry (ICP-OES) (Agilent 725, Agilent Technologies) evaluation.

For distribution study, glioma-bearing nude mice were administered with 100 μL BMP with a Mn dose of 5 mg/kg intravenously and sacrificed after 4 h. Their major organs as well as tumor were excised, weighted, and further digested for ICP-OES assessment.

2.10 Imaging of hypoxia improvement *in vitro* and *in vivo*

The hypoxyprobe kit was adopted to evaluate the ability of the BMP nanoplatform in hypoxia improvement. At the cellular level, four groups, including normoxia group, hypoxia group, hypoxia+BMP group, and hypoxia+BMP+H_2O_2 group, have been assigned. In brief, C6 cells were cultured under hypoxic environment for 2 h with a O_2 content of < 0.1%, which was induced by the AnaeroPack™-Anaero and further confirmed with a Anaero-indicator. BMP (200 μg/mL) and H_2O_2 (100 μM) were added in the hypoxia+BMP group and hypoxia+BMP+H_2O_2 group, respectively. Normoxia group was set as a contrast with routine culture condition. Then, cells were fixed as well as conducted following the kit instruction, and further stained with DAPI for CLSM observation.

Nude mice with subcutaneous glioma were randomly divided into control group and BMP group (n = 3). BMP solution was injected intravenously with a Mn dose of 5 mg/kg, whereas control group was injected with 100 μL NS. 200 μL pimonidazole hydrochloride (60 mg/kg) was intraperitoneally administered after 6 h. Tumors were collected 1.5 h later, and incubated with CD 31, MAb-4.3.11.3, and FITC-HRP, followed by CY3-labelled Donkey anti-goat and FITC-labelled Donkey anti-rabbit IgG as secondary antibodies. After stained with DAPI, CLSM was conducted for hypoxia visualization.

2.11 Anti-cancer effect *in vivo*

Subcutaneous glioma-bearing nude mice were established and randomly divided into 5 groups (n = 5), including control group, BMP group, HIFU group, HIFU+PpIX group, and HIFU+BMP group. The intravenous injection doses of BMP and PpIX were both 5 mg/kg. For HIFU parameters, the intensity was set as 8.5 W/cm^2 with a duration of 20 s. The weight and tumor volume of mice were recorded every other day until tumor volume approximately reached 2,000 mm^3. When the course ended, the harvested tumors were analyzed with H&E and terminal-deoxynucleotide transferase mediated nick end labeling (TUNEL) staining using inverted fluorescence microscope. The quantification for tumor apoptosis was executed with the ImageJ software. Major organs were stained with H&E staining for histological estimation. Moreover, to overall assess the therapeutic outcome, survival evaluation was further performed in glioma-bearing mice (n = 6). The primary composite endpoint was the censored tumor volume or death, and the Kaplan–Meier survival curve was determined within 45 days.

2.12 Statistical analysis

All statistical analyses were executed with IBM SPSS (version 20.0, Chicago, USA) and GraphPad prism (version 7.0, California, USA). Measurement data were expressed as mean ± standard deviation (SD). The differences were compared with Student's t-test or one-way analysis of variance (ANOVA), as appropriate. A p value of < 0.050 was considered statistically significant, whereas n.s. was represented as insignificance.

3 Results and discussion

3.1 Synthesis and characterization of BMP

The BMP was constructed through a facile *in situ* synthesis strategy to obtain BM, followed by conjugating with PpIX via amide reaction (Scheme 1). The impacts of certain experimental parameters on BM characters were explored with UV–vis and dynamic light scattering (DLS) (Fig. S1 in the Electronic Supplementary Material (ESM)). A molar ratio of reactants (BSA/$MnCl_2$) for BM fabrication was eventually assigned as 1:40, offering an optimal particle size of 24.4 nm (Fig. 1(b)). The BM was further anchored with a sonosensitizer of PpIX to obtain the resultant BMP. As revealed by TEM images, both BM and BMP exhibited a monodispersed and regular spherical morphology (Fig. 1(a) and Fig. S2 in the ESM). Compared with BM, the BMP nanoplatform possesses an increased diameter of 50.3 ± 1.3 nm and an approximate zeta potential of −18 ± 0.32 mV (Figs. 1(b) and 1(c)). The hydrodynamic size of BMP remained steady for 21 days in PBS (Figs. S3(a) and S3(b) in the ESM), and its stability in DDW, PBS, FBS, and DMEM solution was also confirmed via

UV–vis spectra (Figs. S3(c) and S3(d) in the ESM). As illustrated by the Fourier transform infrared (FTIR) spectra (Fig. 1(d)), the absorbance peaks of BMP at 1,650 and 1,540 cm^{-1} indicate the N–H stretching, ascribing to the template of BSA for the versatile nanoplatform. XRD analysis in Fig. S4 in the ESM displayed the structure of BMP with diffraction peaks at about 36.3° and 65.4°, indicating the successful growth of MnO_2 *in situ*. Compared with BM, the distinct absorption peak of BMP at about 400 nm represented the successful modification of PpIX (Fig. 1(e)). In addition, a relatively flat emission peak within the wavelength range of about 600–750 nm, which could be attributed to the anchored PpIX, was found in the FS of BMP, compared with that of BM (Fig. S5 in the ESM). As shown in Fig. 1(f), XPS pattern of Mn 2p spectrum appeared two obvious peaks located at 642.19 and 653.99 eV, corresponding to the characteristic of Mn(Ⅳ) $2p_{3/2}$ and Mn(Ⅳ) $2p_{1/2}$, respectively, suggesting the presence of MnO_2 in BMP. Besides, Mn 3s spectrum in Fig. S6 in the ESM showed the energy separation (ΔE) is about 4.88 eV, which also indicates the oxidation state of Mn(Ⅳ). When temperature reached to 800 °C, TGA analysis revealed ~ 22.64 wt% BM was preserved while only ~ 18.43 wt% BMP remained, indicating the loading content of PpIX was ~ 88.40 wt% (Fig. 1(g)).

3.2 O_2 and $^1O_2$ generative capability *in vivo*

In the presence of H_2O_2, MnO_2 could be reduced into Mn^{2+}, contributing to the decomposition of H_2O_2 for O_2 generation [44]. When BMP was added, the content of H_2O_2 decreased, with a BMP concentration-dependent manner, indicating H_2O_2 could be consumed by MnO_2 (Fig. S7 in the ESM). As shown in Fig. S8 in the ESM, the stable absorbances of BMP in PBS at different pH values (pH = 6.5 or 7.4) decreased when incubated with H_2O_2, especially in the simulative TME. Consistently, the O_2 production displayed prominent increase in comparison to that in the simulative physiological environment, which may be a favor for the hypoxia alleviation in the TME (Fig. 1(h)).

The following ROS generative capability of BMP was tested using FS and ESR. After ultrasound irradiation, fluorescence intensity of BMP in the simulative TME was dramatically elevated, whereas mild increment was found for that in the neutral solution (Fig. S9 in the ESM). It may be ascribed to the abundance of O_2 supplied from the effective degradation of MnO_2 in the weak acidic environment to produce $^1O_2$ reasonably. Moreover, the $^1O_2$ generation for the BMP+US+H_2O_2 group was further verified by the detected ESR signal intensity, while only little signals were found for the both BMP group and US group (Fig. 1(i)). Collectively, the propitious conjugation of PpIX in BMP empowered the transfer of O_2 into $^1O_2$ when expose to ultrasound, and the high-efficacy SDT could be achieved in the TME.

3.3 Self-enhanced MRI performance *in vitro* and *in vivo*

On account of the TME-responsive reducibility of MnO_2, the generated dissociative Mn^{2+} ion, as a paramagnetic substance, potentially bestows bioimaging capability on BMP [20]. To evaluate its T_1-weight MRI performance, T_1 signals of BMP at different settings were measured to determine the longitudinal relaxation rate (r_1). As shown in Figs. 2(a) and 2(b), accompanied with the decrease of solution pH from 7.4 to 5.0, the calculated r_1 relaxivity of BMP rose from 1.55 to 4.14 $mM^{-1}·s^{-1}$ correspondingly, attributing to the pH-responsive enhancement on T_1WI. In particular, the r_1 relaxivity significantly elevated in the presence of H_2O_2, with an approximate r_1 value of 9.76 $mM^{-1}·s^{-1}$ under the stimulated TME, a 5.3-fold increasement compared to the physiological condition. Except the pH- and H_2O_2-dependent manifestations, the signal intensity on T_1WI also presented a

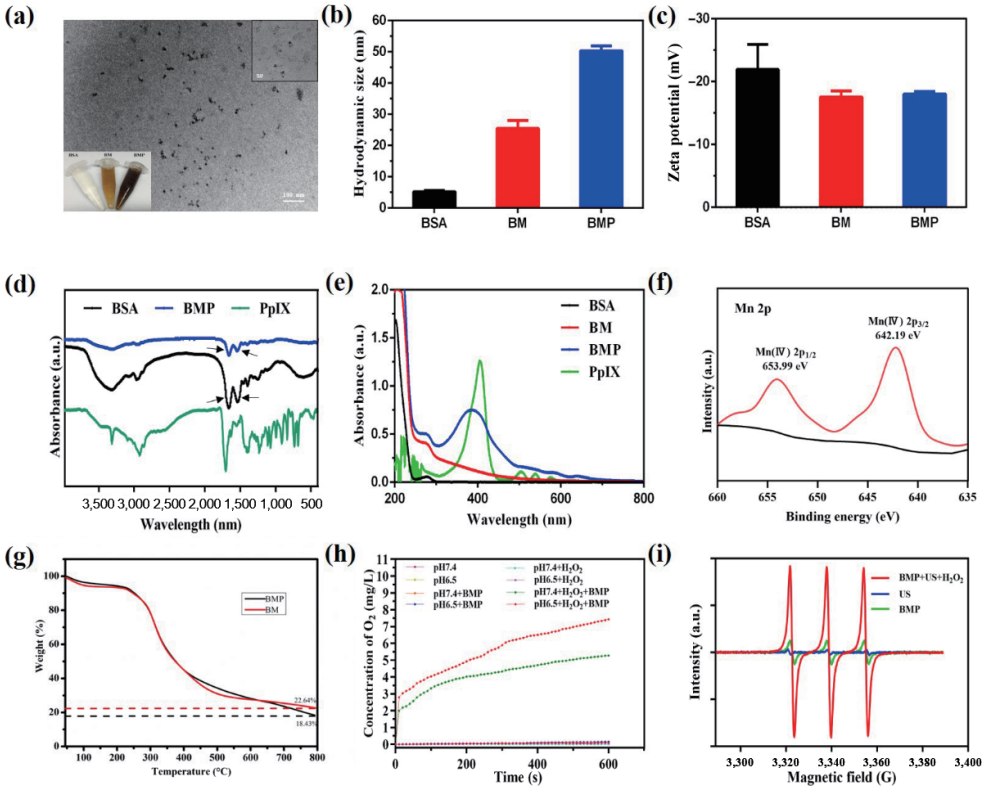

Figure 1 Characterization of BMP. (a) TEM image of BMP with the indicating scale bar of 100 nm. The right upper inset is the amplifying micrograph with the scale bar of 20 nm. The left lower inset is the digital photograph of BSA, BM, and BMP, respectively. (b) The respective hydrodynamic size and (c) zeta potential of BSA, BM, and BMP. (d) FTIR spectra of BSA, BMP, and PpIX. Black arrow indicates the amide bond at 1,650 and 1,540 cm^{-1}, respectively. (e) UV–vis spectra of BSA, BM, BMP, and PpIX. (f) XPS spectrum of Mn 2p for BMP. (g) TGA of BM and BMP. (h) O_2 generative curves of BMP under different pH conditions, with or without the presence of H_2O_2. (i) ESR spectra of US group, BMP group, and BMP+US+H_2O_2 group.

positive Mn concentration dependence, especially for the acid and/or H_2O_2-containing groups. These *in vitro* results demonstrate the potential capability of BMP on tumor targeting detection, which may be eligible as an MRI CA for imaging-guided high-efficacy SDT.

Then, C6 cells were employed to further validate the self-enhanced imaging property of BMP. On T_1WI, the signals of glioma cells incubated with BMP-containing medium were statistical significantly higher than that cultured with DMEM medium, or pure BMP solution as well as DMEM medium, which verified the bioresponsive MRI performance at the cellular level (Fig. 2(c)). In addition, T_1 signals were enriched as the increment of incubated time or BMP concentration, illustrating the time- and Mn concentration-dependent manner on imaging (Fig. S10 in the ESM).

Delighted by the above discoveries *in vitro*, the feasibility of BMP bioimaging *in vivo* was subsequently explored in glioma-bearing animal models. The MRI performances of BMP and Gd-DTPA were evaluated in rats with orthotopic gliomas. As revealed in Figs. 2(d) and 2(f), and Fig. S11 in the ESM, despite the similar tumor reinforcement, conspicuous hyperintensity was observed for 1 h and remained visible for 4 h after intravenous injection of BMP, whereas prompt high T_1 signal emerged at 5 min but was washed out 2 h later for the Gd-DTPA group. The trend of determined SNR was consistent with MR manifestations, substantiating that BMP, with BSA as the nanovehicle, holds the competence in delayed clearance in the blood circulation, contributing to the prolonged enhancement window compared with the commercial CA. Most notably, in contrast to the discernible enhancement on adjacent muscles for the Gd-DTPA group, there was no statistical difference among the SNRs after BMP injection (Fig. 2(g)). However, a 3-fold increasement of CNR was exhibited in BMP-injected tumor (Fig. 2(h)), which suggests the TME-responsive property could strengthen the contrast between glioma and surrounding structures for specific MR imaging. Afterwards, mouse bearing with subcutaneous glioma underwent tail-vein administration of BMP was examined. As shown in Figs. 2(e) and 2(i), T_1 signals reached the highest for 2 h, and the tumor region was still brightened even for 24 h, with slightly enhanced muscles at each timepoint, further proving the qualification of BMP on contrast improvement to realize spatiotemporal controllability of MRI guidance.

3.4 Cytotoxicity and phagocytosis *in vitro*

The cytotoxicity of BMP under different cultured environments was measured by CCK-8 assay. After 24 h of incubation, BMP demonstrated a favorable biocompatibility against C6 cells, and little influence was observed under the simulative physiological environment within the given concentrations from 25–600 μg/mL. Even when BMP was at a high concentration of 600 μg/mL, the survival rate under the TME was slightly decreased to 77.3% merely (Fig. 3(a)). Furthermore, the impact of HIFU parameters on cellular variability, including intensity and duration, was investigated. As shown in Fig. S12 in the ESM, a HIFU intensity of 8.5 W/cm^2 with a duration of 1.5 min possessed a negative cytotoxicity on C6 cells, and thus, it was selected as the therapeutic project for the following experiments.

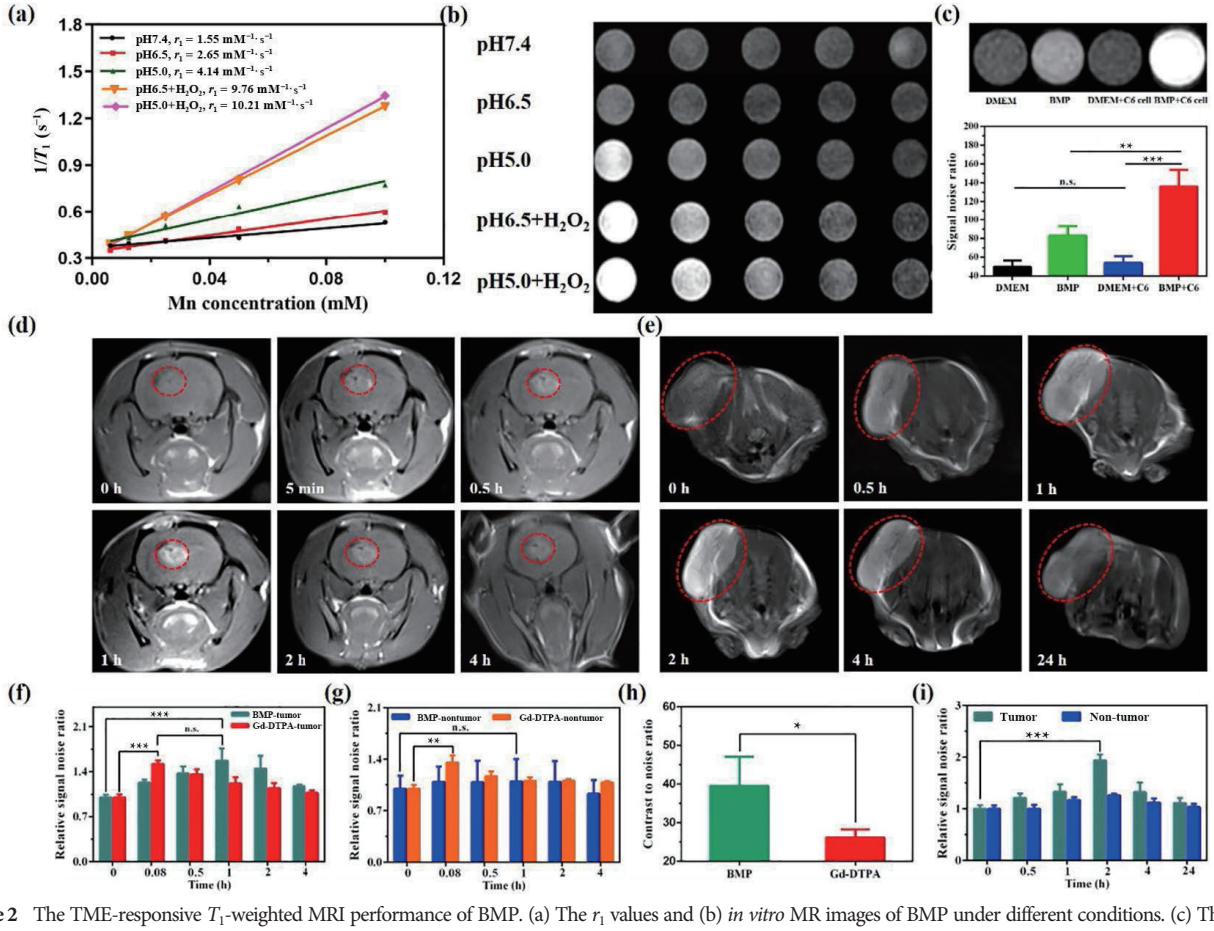

Figure 2 The TME-responsive T_1-weighted MRI performance of BMP. (a) The r_1 values and (b) *in vitro* MR images of BMP under different conditions. (c) The MR images and SNR results of DMEM media, BMP solution, C6 cells incubated with DMEM medium as well as BMP-containing medium. *In vivo* T_1WI of the orthotopic (d) and subcutaneous (e) glioma models examined at various time points after intravenous injection of BMP. The SNR results of (f) tumor region and (g) non-tumor region after BMP or Gd-DTPA administration in orthotopic glioma-bearing rats. (h) The CNR results of BMP and Gd-DTPA. (i) The SNR results of tumor area and non-tumor area in nude mice with xenograft after BMP infection.

As a fluorescent dye, FITC was labelled on the surface of BMP to trace the cellular internalization by C6 cells. The flow cytometry analysis and CLSM examination were also conducted. Flow cytometry analysis quantificationally elucidated a time-dependent increase of fluorescence intensity, with a significant difference after 2 h of coincubation in statistics, which further enhanced at 4 h assessment (Figs. 3(b) and 3(c)). Besides, efficient cellular phagocytosis was also evidenced by CLSM observation, in which green fluorescence gradually became stronger in the cytoplasm following the extended time (Fig. 3(d)).

3.5 *In vitro* therapeutic efficiency and detection of ROS generation

To explore the therapeutic efficiency of BMP against C6 cells, CCK-8 assay was adopted. As illustrated in Fig. 3(e), after HIFU exposure, cell viability showed a concentration-dependent inhibition under the simulative environment containing H_2O_2 and neutral media. Importantly, it was further depressed under the TME, with a suppressive rate of 83.4% at a BMP concentration of 200 μg/mL, which was statistically higher than that of 30.5% in the neutral environment. Calcein-AM/PI dual-staining was further applied to observe the cell status with CLSM. The C6 cells were compatible in the BMP+H_2O_2+pH7.4 group, and slightly inhibited when irradiated by HIFU only, as evidenced in Fig. 3(f). Most notably, cell death was more prominent in the simulative TME after treated with BMP followed by HIFU irradiation, compared with that in the BMP+HIFU+H_2O_2+pH7.4 group. These results confirmed BMP is capable of eliminating cells upon HIFU treatment, and its therapeutic efficacy could be specifically enhanced at tumor site.

The mechanism in cell apoptosis was subsequently investigated by characterizing intracellular $^1O_2$ levels using DCFH-DA probe. As shown in Fig.3(g), abundance of $^1O_2$ was observed only when cells received BMP combined with HIFU therapy, and the ROS production was more obvious in the BMP+HIFU+H_2O_2+pH6.5 group, as verified by the stronger green fluorescence in the

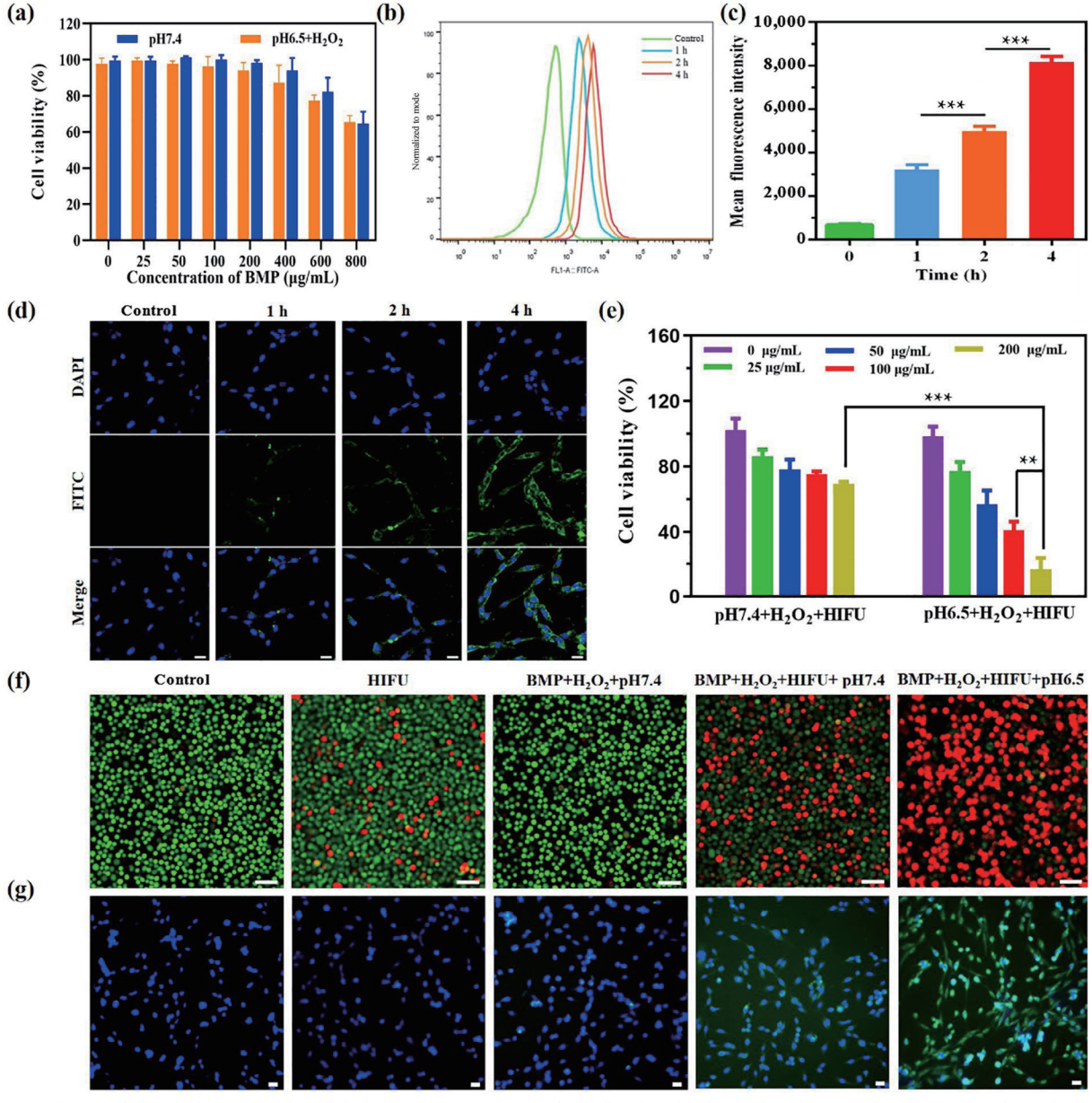

Figure 3 Evaluation of BMP performance at the cellular level. (a) The cytotoxicity of C6 cells cultured with varied concertation of BMP under simulative physiological environment (pH7.4) or TME (H_2O_2+pH6.5). (b) Flow cytometry analysis with (c) corresponding fluorescence intensity of cellular uptake of BMP. (d) Confocal images of C6 cellular uptake of BMP at varied timepoints. Scale bar = 20 μm. (e) Concentration-dependent cytotoxity of C6 cell after different treatments. (f) CLSM analyses of cellular apoptosis under various conditions. Scale bar = 50 μm. (g) Confocal images of ROS generation under different managements. Scale bar = 20 μm.

cytoplasm. The semiquantitative analysis in Fig. S13 in the ESM also confirmed the CLSM results. After BMP and HIFU treatment, the relative fluorescence intensity representing ROS level statistically increased under the weak acid environment in C6 cells, compared with that of simulative physiological environment. Therefore, the efficient cell damage could be reasonably ascribed to the excellent sonosensitizer capability of BMP on converting O_2 into ROS under the special TME.

3.6 *In vivo* biocompatibility, pharmacokinetic, and distribution studies

The biocompatibility assays, including hemocompatibility and histocompatibility, were conducted to evaluate the systemic toxicity of BMP. As shown in Fig. S14 in the ESM, there were no obvious body-weight losses during the observation period. Besides, no distinct abnormality was noticed in blood indexes compared with the control group, implying that BMP has negligible impacts on hematologic, liver as well as renal function. The H&E staining results also confirmed the negative effect of BMP *in vivo*, with negative histopathological changes in the major organs. The pharmacokinetic behavior of BMP was estimated by tracing the Mn concentration in the blood circulation. After injected with BMP, the Mn content diminished rapidly in the first 30 min, and the residue was below 1 μg till 8 h (Fig. S15(a) in the ESM). The biodistribution of BMP, in addition, was measured with ICP-OES, and the dominating accumulation was detected in the liver and kidney, which conforms with the pattern of small sized nanoparticle (Fig. S15(b) in the ESM) [45].

3.7 Improvement of hypoxic microenvironment *in vitro* and *in vivo*

Hypoxia, a well-established hallmark of the TME, resulting from an imbalance between undersupply and over-consumption of O_2, governs diverse tumor processes such as neovascularization, proliferation, invasiveness, metastasis, and chemo/radio-resistance [46, 47]. Considering the efficient O_2 production *in vitro*, the improvement of hypoxic microenvironment by BMP was imaged at the cellular level firstly. As shown in Fig. S16(a) in the ESM, compared with normoxia group, obvious green fluorescence representing the hypoxic condition was detected in the hypoxic cells. The hypoxia was slightly alleviated in the hypoxia+BMP group, while it was significantly improved after treated with BMP and H_2O_2, ascribing to the generation of O_2 under the similative TME. Moreover, the semiquantitative results were consistent with quantitative observations, as displayed in Fig. S16(b) in the ESM.

The ability of BMP in improving hypoxia was further estimated on mice bearing with glioma. After injection of BMP, the green fluorescence of hypoxia region was decreased in comparison with the control group, with the approximate vascular as well as cellular fluorescence between the two groups, indicating the instrumental effect of BMP on O_2 modulation (Fig. 4(a)). The semiquantitative analysis in Fig. 4(b) further certified the dramatically reduced green fluorescence intensity in the BMP group, in accordance with the CLSM manifestations.

3.8 Therapeutic efficacy of BMP *in vivo*

Excellent performance of ROS-inducing therapeutic response in glioma cells by BMP necessitated estimating the efficacy of MRI-guided SDT *in vivo*. As illustrated in Figs. 4(c) and 4(d), rats administrated with BMP only showed little decrease in tumor volume and weight indicative of little toxicity of the nanocomposite alone. In contrast, compared with the others, including the HIFU group and HIFU+PpIX group, BMP combined with HIFU therapy showed the most prominent suppression on tumor growth, reasonably owing to the hypoxia alleviation in the TME and substrate supplementary for $^1O_2$ generation by BMP. The tumor photographs were in consistent with the aforementioned results of tumor volume and weight (Fig. 4(e)). The Kaplan–Meier survival curves revealed the PpIX combined with HIFU therapy could partially improve the outcome when compared with the control group, BMP group, and HIFU group, but glioma-bearing mice all died within 39 days. Notably, the survival time of mice received with the high-efficacy SDT was significantly prolonged, in which the survival rate maintained 100% even till the censored date (Fig. 4(f)). Besides, no noticeable change was observed in the bodyweight, as well as H&E staining of the major organs during the treatment (Figs. S17 and S18 in the ESM).

To elucidate the potential mechanisms underlying the antitumor effect, histopathological performances within the tumor region were investigated. As expected, obvious adverse abnormalities in the H&E staining, including cytoplasmic vacuolation, nucleus condensation and fragmentation, as well as necrocytosis, were found in the HIFU group, HIFU+PpIX group, and HIFU+BMP group, especially for the HIFU+BMP group (Fig. 4(g)). Besides, much more tumor necrosis was also manifested in the HITU+BMP group with stronger and broader green fluorescence. Compared with HIFU therapy alone, the mean FITC intensity representing tumor apoptosis significantly increased in the HIFU+PpIX group, and it further statistically elevated when tumor received with BMP and HIFU therapy, as quantified in the semiquantitative analysis (Fig. S19 in the ESM). These findings suggest the combination of HIFU and BMP could augment the therapeutic effect of HIFU to achieve the high-efficacy SDT.

4 Conclusions

A versatile nanocomposite BMP was prepared to augment HIFU efficiency for TME-responsive MRI-guided SDT, in which MnO_2 was *in situ* grown into BSA followed by PpIX conjugation. The degradation of BMP in response to the TME contributes to Mn^{2+} release for specific T_1-weighted MRI to visualize glioma. Besides, the high reactivity of MnO_2 toward H_2O_2 simultaneously generates O_2 to alleviate tumor hypoxia, and further enhance the therapeutic efficiency of SDT under HIFU by facilitating $^1O_2$ production, thereby realizing the efficient glioma suppression. Considering the facile synthesis procedure, *in situ* MRI capacity, satisfactory antitumor effect, and favorable biocompatibility, this research provides a promising perspective for enhanced SDT in glioma treatment with potential clinical translation.

Acknowledgements

The authors thank Dalong Ni, at Ruijin Hospital, Shanghai Jiao Tong University School of Medicine, Shanghai, China, for manuscript editing. We are also grateful to Minxia Wu, at Fujian Medical University, Fuzhou, China, for her assistance in nanoparticle characterization. This work was financially supported by the Shanghai Municipal Science and Technology Major Project (No. 2018SHZDZX01) and ZJ Lab, Shanghai Center for Brain-Inspired Technology, and the Youth Program of National Natural Science Foundation of China (No. 81901697).

Electronic Supplementary Material: Supplementary material (physical and chemical property, MRI performance, biosafety evaluation of samples, quantification for cellular ROS production and tumor apoptosis, and cellular hypoxia evaluation) is available in the online version of this article at https://doi.org/10.1007/s12274-022-4542-9.

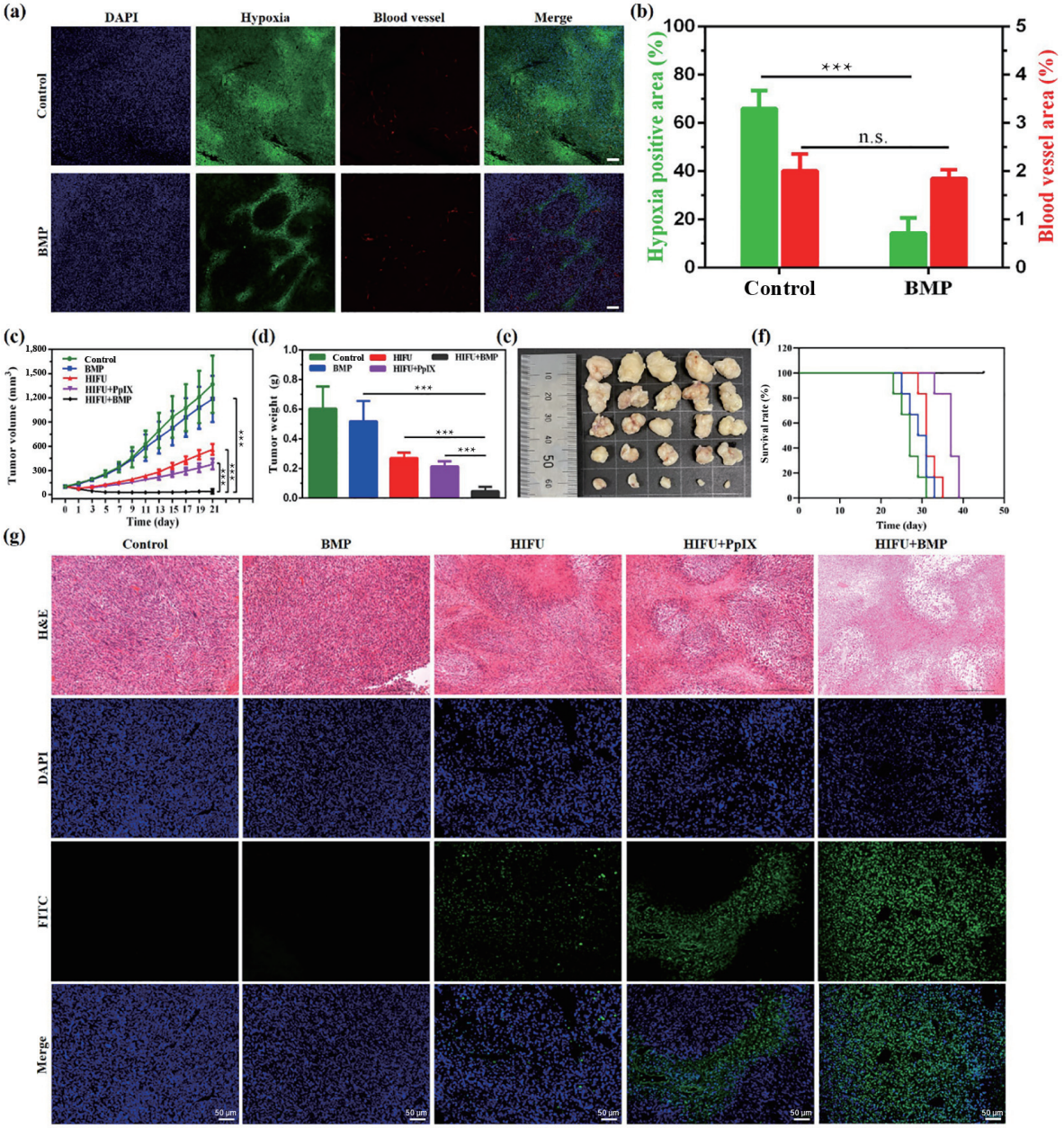

Figure 4 Evaluation of BMP performance *in vivo*. (a) Confocal images and (b) semiquantitative analysis of tumor hypoxic evaluation with or without BMP treatment. (c) Tumor volume curves, (d) weight, (e) photograph, and (f) the Kaplan–Meier curves of glioma-bearing mice with different treatments. (g) H&E and TUNEL staining of tumor tissues after various treatments. Scale bar = 50 μm.

References

[1] Nabors, L. B.; Portnow, J.; Ahluwalia, M.; Baehring, J.; Brem, H.; Brem, S.; Butowski, N.; Campian, J. L.; Clark, S. W.; Fabiano, A. J. et al. Central nervous system cancers, version 3.2020, NCCN clinical practice guidelines in oncology. *J. Natl. Compr. Canc. Netw.* **2020**, *18*, 1537–1570.

[2] Pace, A.; Dirven, L.; Koekkoek, J. A. F.; Golla, H.; Fleming, J.; Rudà, R.; Marosi, C.; Le Rhun, E.; Grant, R.; Oliver, K. et al. European association for neuro-oncology (EANO) guidelines for palliative care in adults with glioma. *Lancet Oncol.* **2017**, *18*, e330–e340.

[3] Lapointe, S.; Perry, A.; Butowski, N. A. Primary brain tumours in adults. *Lancet* **2018**, *392*, 432–446.

[4] Armstrong, T. S.; Dirven, L.; Arons, D.; Bates, A.; Chang, S. M.; Coens, C.; Espinasse, C.; Gilbert, M. R.; Jenkinson, D.; Kluetz, P. et al. Glioma patient-reported outcome assessment in clinical care and research: A response assessment in neuro-oncology collaborative report. *Lancet Oncol.* **2020**, *21*, e97–e103.

[5] Alkins, R. D.; Mainprize, T. G. High-intensity focused ultrasound ablation therapy of gliomas. *Prog. Neurol. Surg.* **2018**, *32*, 39–47.

[6] Van Den Bijgaart, R. J. E.; Eikelenboom, D. C.; Hoogenboom, M.; Fütterer, J. J.; Den Brok, M. H.; Adema, G. J. Thermal and mechanical high-intensity focused ultrasound: Perspectives on tumor ablation, immune effects and combination strategies. *Cancer Immunol. Immunother.* **2017**, *66*, 247–258.

[7] Hsiao, Y. H.; Kuo, S. J.; Tsai, H. D.; Chou, M. C.; Yeh, G. P. Clinical application of high-intensity focused ultrasound in cancer therapy. *J. Cancer* **2016**, *7*, 225–231.

[8] Chen, Y.; Chen, H. R.; Shi, J. L. Nanobiotechnology promotes noninvasive high-intensity focused ultrasound cancer surgery. *Adv. Healthcare Mater.* **2015**, *4*, 158–165.

[9] Zhang, X. M.; Zheng, Y. Y.; Wang, Z. G.; Huang, S.; Chen, Y.; Jiang, W.; Zhang, H.; Ding, M. X.; Li, Q. S.; Xiao, X. Q. et al. Methotrexate-loaded PLGA nanobubbles for ultrasound imaging and synergistic targeted therapy of residual tumor during HIFU ablation. *Biomaterials* **2014**, *35*, 5148–5161.

[10] Bilmin, K.; Kujawska, T.; Grieb, P. Sonodynamic therapy for gliomas. Perspectives and prospects of selective sonosensitization of glioma cells.. *Cells* **2019**, *8*, 1428.

[11] Son, S. B.; Kim, J. H.; Wang, X. W.; Zhang, C. L.; Yoon, S. A.; Shin, J.; Sharma, A.; Lee, M. H.; Cheng, L.; Wu, J. S. et al. Multifunctional sonosensitizers in sonodynamic cancer therapy. *Chem. Soc. Rev.* **2020**, *49*, 3244–3261.
[12] Liang, S.; Deng, X. R.; Ma, P. A.; Cheng, Z. Y.; Lin, J. Recent advances in nanomaterial-assisted combinational sonodynamic cancer therapy. *Adv. Mater.* **2020**, *32*, 2003214.
[13] Lin, X. H.; Song, J. B.; Chen, X. Y.; Yang, H. H. Ultrasound-activated sensitizers and applications. *Angew. Chem., Int. Ed.* **2020**, *59*, 14212–14233.
[14] Xu, M. M.; Zhou, L. Q.; Zheng, L.; Zhou, Q.; Liu, K.; Mao, Y. H.; Song, S. S. Sonodynamic therapy-derived multimodal synergistic cancer therapy. *Cancer Lett.* **2021**, *497*, 229–242.
[15] Liu, Y. C.; Bai, L. M.; Guo, K. L.; Jia, Y. L.; Zhang, K.; Liu, Q. H.; Wang, P.; Wang, X. B. Focused ultrasound-augmented targeting delivery of nanosonosensitizers from homogenous exosomes for enhanced sonodynamic cancer therapy. *Theranostics* **2019**, *9*, 5261–5281.
[16] Fite, B. Z.; Wang, J.; Ghanouni, P.; Ferrara, K. W. A review of imaging methods to assess ultrasound-mediated ablation. *BME Front.* **2022**, *2022*, 9758652.
[17] Kuroda, K. MR techniques for guiding high-intensity focused ultrasound (HIFU) treatments. *J. Magn. Reson. Imaging* **2018**, *47*, 316–331.
[18] Smith, B. R.; Gambhir, S. S. Nanomaterials for *in vivo* imaging. *Chem. Rev.* **2017**, *117*, 901–986.
[19] Kunjachan, S.; Ehling, J.; Storm, G.; Kiessling, F.; Lammers, T. Noninvasive imaging of nanomedicines and nanotheranostics: Principles, progress, and prospects. *Chem. Rev.* **2015**, *115*, 10907–10937.
[20] Ding, B. B.; Zheng, P.; Ma, P. A.; Lin, J. Manganese oxide nanomaterials: Synthesis, properties, and theranostic applications. *Adv. Mater.* **2020**, *32*, 1905823.
[21] Cai, X. X.; Zhu, Q. X.; Zeng, Y.; Zeng, Q.; Chen, X. L.; Zhan, Y. H. Manganese oxide nanoparticles as mri contrast agents in tumor multimodal imaging and therapy. *Int. J. Nanomedicine* **2019**, *14*, 8321–8344.
[22] Chen, Z. W.; Jiao, Z.; Pan, D. Y.; Li, Z.; Wu, M. H.; Shek, C. H.; Wu, C. M. L.; Lai, J. K. L. Recent advances in manganese oxide nanocrystals: Fabrication, characterization, and microstructure. *Chem. Rev.* **2012**, *112*, 3833–3855.
[23] Li, Y.; Zhao, X.; Liu, X. L.; Cheng, K. M.; Han, X. X.; Zhang, Y. L.; Min, H.; Liu, G. N.; Xu, J. C.; Shi, J. et al. A bioinspired nanoprobe with multilevel responsive T_1-weighted MR signal-amplification illuminates ultrasmall metastases. *Adv. Mater.* **2020**, *32*, 1906799.
[24] Ji, T. J.; Zhao, Y.; Ding, Y. P.; Nie, G. J. Using functional nanomaterials to target and regulate the tumor microenvironment: Diagnostic and therapeutic applications. *Adv. Mater.* **2013**, *25*, 3508–3525.
[25] Wu, T.; Dai, Y. Tumor microenvironment and therapeutic response. *Cancer Lett.* **2017**, *387*, 61–68.
[26] Fu, C. P.; Duan, X. H.; Cao, M. H.; Jiang, S. Q.; Ban, X. H.; Guo, N.; Zhang, F.; Mao, J. J.; Huyan, T.; Shen, J. et al. Targeted magnetic resonance imaging and modulation of hypoxia with multifunctional hyaluronic acid-MnO_2 nanoparticles in glioma. *Adv. Healthcare Mater.* **2019**, *8*, 1900047.
[27] Zhu, P.; Chen, Y.; Shi, J. L. Nanoenzyme-augmented cancer sonodynamic therapy by catalytic tumor oxygenation. *ACS Nano* **2018**, *12*, 3780–3795.
[28] Xu, Q. B.; Zhan, G. T.; Zhang, Z. L.; Yong, T. Y.; Yang, X. L.; Gan, L. Manganese porphyrin-based metal-organic framework for synergistic sonodynamic therapy and ferroptosis in hypoxic tumors. *Theranostics* **2021**, *11*, 1937–1952.
[29] Cui, X. W.; Han, X. X.; Yu, L. D.; Zhang, B.; Chen, Y. Intrinsic chemistry and design principle of ultrasound-responsive nanomedicine. *Nano Today* **2019**, *28*, 100773.
[30] Li, Z.; Tan, S. R.; Li, S.; Shen, Q.; Wang, K. H. Cancer drug delivery in the nano era: An overview and perspectives (Review). *Oncol. Rep.* **2017**, *38*, 611–624.
[31] Amreddy, N.; Babu, A.; Muralidharan, R.; Panneerselvam, J.; Srivastava, A.; Ahmed, R.; Mehta, M.; Munshi, A.; Ramesh, R. Recent advances in nanoparticle-based cancer drug and gene delivery. *Adv. Cancer Res.* **2018**, *137*, 115–170.
[32] Patel, S.; Ashwanikumar, N.; Robinson, E.; DuRoss, A.; Sun, C.; Murphy-Benenato, K. E.; Mihai, C.; Almarsson, Ö.; Sahay, G. Boosting intracellular delivery of lipid nanoparticle-encapsulated mRNA. *Nano Lett.* **2017**, *17*, 5711–5718.
[33] Kratz, F. Albumin as a drug carrier: Design of prodrugs, drug conjugates and nanoparticles. *J. Control. Release* **2008**, *132*, 171–183.
[34] Chen, J. W.; Chen, Q.; Liang, C.; Yang, Z. J.; Zhang, L.; Yi, X.; Dong, Z. L.; Chao, Y.; Chen, Y. G.; Liu, Z. Albumin-templated biomineralizing growth of composite nanoparticles as smart nano-theranostics for enhanced radiotherapy of tumors. *Nanoscale* **2017**, *9*, 14826–14835.
[35] Chen, Q.; Liu, Z. Albumin carriers for cancer theranostics: A conventional platform with new promise. *Adv. Mater.* **2016**, *28*, 10557–10566.
[36] Chen, B.; He, X. Y.; Yi, X. Q.; Zhuo, R. X.; Cheng, S. X. Dual-peptide-functionalized albumin-based nanoparticles with ph-dependent self-assembly behavior for drug delivery. *ACS Appl. Mater. Interfaces* **2015**, *7*, 15148–15153.
[37] Chen, Q.; Feng, L. Z.; Liu, J. J.; Zhu, W. W.; Dong, Z. L.; Wu, Y. F.; Liu, Z. Intelligent albumin-MnO_2 nanoparticles as pH-/H_2O_2-responsive dissociable nanocarriers to modulate tumor hypoxia for effective combination therapy. *Adv. Mater.* **2016**, *28*, 7129–7136.
[38] Elzoghby, A. O.; Samy, W. M.; Elgindy, N. A. Albumin-based nanoparticles as potential controlled release drug delivery systems. *J. Control. Release* **2012**, *157*, 168–182.
[39] Lin, T. T.; Zhao, P. F.; Jiang, Y. F.; Tang, Y. S.; Jin, H. Y.; Pan, Z. Z.; He, H. N.; Yang, V. C.; Huang, Y. Z. Blood-brain-barrier-penetrating albumin nanoparticles for biomimetic drug delivery via albumin-binding protein pathways for antiglioma therapy. *ACS Nano* **2016**, *10*, 9999–10012.
[40] Yang, W. T.; Guo, W. S.; Le, W. J.; Lv, G. X.; Zhang, F. H.; Shi, L.; Wang, X. L.; Wang, J.; Wang, S.; Chang, J. et al. Albumin-bioinspired Gd: CuS nanotheranostic agent for *in vivo* photoacoustic/magnetic resonance imaging-guided tumor-targeted photothermal therapy. *ACS Nano* **2016**, *10*, 10245–10257.
[41] Chen, Q.; Liang, C.; Wang, C.; Liu, Z. An imagable and photothermal "Abraxane-like" nanodrug for combination cancer therapy to treat subcutaneous and metastatic breast tumors. *Adv. Mater.* **2015**, *27*, 903–910.
[42] Liu, X. Q.; Mohanty, R. P.; Maier, E. Y.; Peng, X. J.; Wulfe, S.; Looney, A. P.; Aung, K. L.; Ghosh, D. Controlled loading of albumin-drug conjugates *ex vivo* for enhanced drug delivery and antitumor efficacy. *J. Control. Release* **2020**, *328*, 1–12.
[43] An, F. F.; Zhang, X. H. Strategies for preparing albumin-based nanoparticles for multifunctional bioimaging and drug delivery. *Theranostics* **2017**, *7*, 3667–3689.
[44] Lin, L. S.; Song, J. B.; Song, L.; Ke, K. M.; Liu, Y. J.; Zhou, Z. J.; Shen, Z. Y.; Li, J.; Yang, Z.; Tang, W. et al. Simultaneous fenton-like ion delivery and glutathione depletion by MnO_2-based nanoagent to enhance chemodynamic therapy. *Angew. Chem., Int. Ed.* **2018**, *57*, 4902–4906.
[45] Zhang, Y. N.; Poon, W.; Tavares, A. J.; McGilvray, I. D.; Chan, W. C. W. Nanoparticle-liver interactions: Cellular uptake and hepatobiliary elimination. *J. Control. Release* **2016**, *240*, 332–348.
[46] Rankin, E. B.; Giaccia, A. J. Hypoxic control of metastasis. *Science* **2016**, *352*, 175–180.
[47] Kumar, V.; Gabrilovich, D. I. Hypoxia-inducible factors in regulation of immune responses in tumour microenvironment. *Immunology* **2014**, *143*, 512–519.